Cell Reports
Physical Science

CellPress
OPEN ACCESS

Article

# Elucidation of the pre-nucleation phase directing metal-organic framework formation

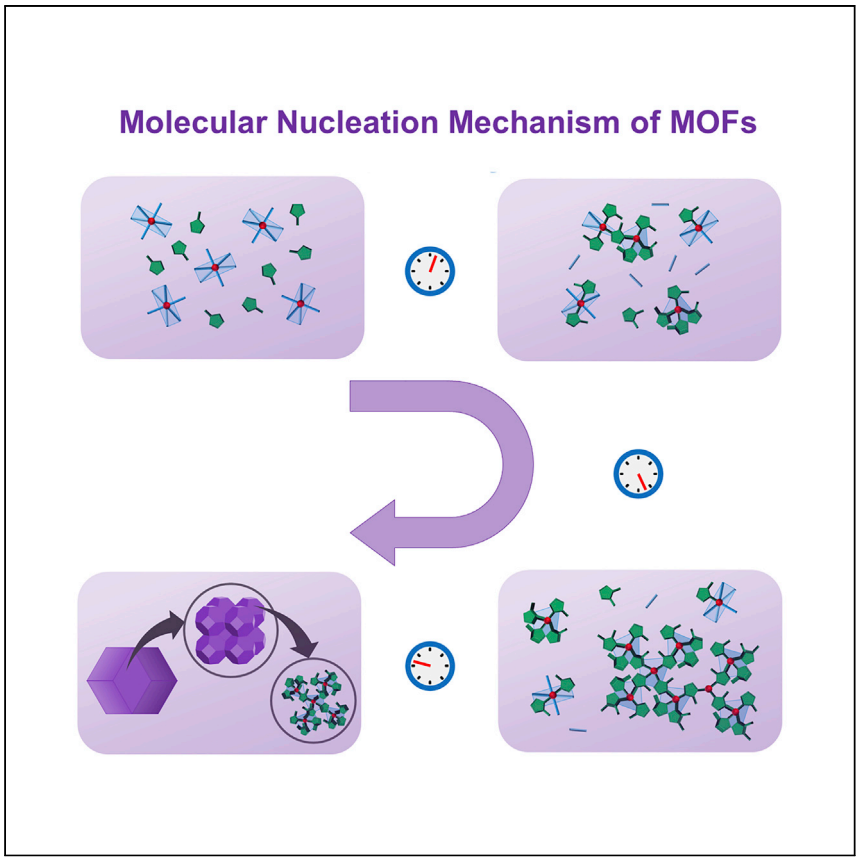


The molecular pathway that governs metal-organic framework formation is challenging to grasp. Filez et al. establish a multi-scale characterization approach combined with theory to link the somewhat different worlds of "molecular" metal-organic ligand assembly and MOF "particle" crystallization.

Matthias Filez, Chiara Caratelli, Miguel Rivera-Torrente, ..., Albert J.R. Heck, Veronique Van Speybroeck, Bert M. Weckhuysen

b.m.weckhuysen@uu.nl

## Highlights

Simultaneous probing of metal-organic complexes, oligomeric nuclei, and MOF particles

Metal-organic pool forms as pre-equilibrium with geometry diverse complexes

"Nucleation" and "growth" complexes are discriminated, which assemble into nuclei

Stable nuclei are observed, growing into MOF particles with autocatalytic kinetics

Filez et al., Cell Reports Physical Science 2, 100680
December 22, 2021 
https://doi.org/10.1016/j.xcrp.2021.100680

Please cite this article in press as: Filez et al., Elucidation of the pre-nucleation phase directing metal-organic framework formation, Cell Reports Physical Science (2021), https://doi.org/10.1016/j.xcrp.2021.100680

Cell Reports
Physical Science

CellPress
OPEN ACCESS

Article

# Elucidation of the pre-nucleation phase directing metal-organic framework formation

Matthias Filez,[1,4,5] Chiara Caratelli,[2] Miguel Rivera-Torrente,[1] Francesco Muniz-Miranda,[2,6] Max Hoek,[3] Maarten Altelaar,[3] Albert J.R. Heck,[3] Veronique Van Speybroeck,[2] and Bert M. Weckhuysen[1,7,*]

## SUMMARY

**Metal-organic framework (MOF) crystallization is governed by molecular assembly processes in the pre-nucleation stage. Yet, unravelling these pre-nucleation pathways and rationalizing their impact on crystal formation poses a great challenge since probing molecular-scale assemblies and macroscopic particles simultaneously is very complex. Herein, we present a multimodal, integrated approach to monitor MOF nucleation across multiple length scales by combining *in situ* optical spectroscopy, mass spectrometry, and molecular simulations. This approach allows tracing initial metal-organic complexes in solution and their assembly into oligomeric nuclei and simultaneously probing particle formation. During Co-ZIF-67 nucleation, a metal-organic pool forms with a variety of complexes caused by ligand exchange and symmetry reduction reactions. We discriminate complexes capable of initiating nucleation from growth species required for oligomerization into frameworks. $Co_4$-nuclei are observed, which grow into particles following autocatalytic kinetics. The geometric and compositional variability of metal-organic pool species clarifies long-debated amorphous zeolitic imidazolate framework (ZIF)-particle nucleation and non-classic pathways of MOF crystallization.**

## INTRODUCTION

Metal-organic frameworks (MOFs) display unparalleled chemical diversity and functionality in their building blocks, providing a unique toolbox to design new application-tailored materials.[1–3] Despite this enormous potential, MOF synthesis mostly presents a laborious, case-by-case endeavor[4–7] based on trial-and-error experimentation instead of predictive synthesis. To speed-up MOF discovery, high-throughput synthesis[8] is often applied to efficiently screen a reaction parameter grid. Yet, such "brute force" methods typically yield only a small subset of computationally[9] and rationally[10] predicted design space. Even when successful MOF synthesis recipes are found, these are not generally transferrable to other MOFs, even within structurally similar families—not suitable for scale-up—since slightly altering the synthesis parameters impacts nucleation conditions and product formation.[5] Therefore, a major leap forward toward predictive synthesis necessitates an in-depth understanding of the general principles underlying MOF crystallization, rather than a case-by-case empirical optimization of synthesis recipes.

Pioneering efforts have been performed in the past decades to decode MOF nucleation by applying a variety of particle-sensitive characterization tools, such as *in situ* small-angle[11,12] and wide-angle[13,14] X-ray scattering (SAXS-WAXS), light

[1]Inorganic Chemistry and Catalysis group, Debye Institute for Nanomaterials Science, Utrecht University, Universiteitsweg 99, 3584 CG Utrecht, the Netherlands

[2]Center for Molecular Modeling, Faculty of Engineering and Architecture, Ghent University, Technologiepark 46, 9052 Zwijnaarde, Belgium

[3]Biomolecular Mass Spectrometry and Proteomics, Bijvoet Center for Biomolecular Research and Utrecht Institute for Pharmaceutical Sciences, Utrecht University, Padualaan 8, 3584 CH Utrecht, the Netherlands

[4]Present address: Conformal Coating of Nanostructures (CoCooN), Ghent University, Krijgslaan 281 (S1), 9000 Ghent, Belgium

[5]Present address: Centre for Membrane Separations, Adsorption, Catalysis and Spectroscopy for Sustainable Solutions (cMACS), KU Leuven, Celestijnenlaan 200F, Leuven 3001, Belgium

[6]Present address: Department of Chemical and Geological Sciences (DSCG), University of Modena and Reggio-Emilia (UniMORE), Via Campi 103, 41125 Modena, Italy

[7]Lead contact

*Correspondence: b.m.weckhuysen@uu.nl

https://doi.org/10.1016/j.xcrp.2021.100680

Please cite this article in press as: Filez et al., Elucidation of the pre-nucleation phase directing metal-organic framework formation, Cell Reports Physical Science (2021), https://doi.org/10.1016/j.xcrp.2021.100680



scattering,[15,16] and transmission electron microscopy[17] (TEM). While these efforts greatly enriched our current understanding of MOF particle nucleation,[5,18] the underlying molecular origins that govern the assembly of (pre-)nuclei and dictate subsequent MOF particle formation have remained largely unknown. In particular, only a limited number of characterization studies detail the molecular assemblies formed in solution mixtures prior to macroscopic MOF formation due to the "extremely challenging"[5] characterization (e.g., by applying pair distribution function[19,20] [PDF], electrospray-ionization mass spectrometry[21,22] [ESI-MS], or nuclear magnetic resonance[23] [NMR]), but a general understanding is lacking. In addition, these characterization studies do not report on the impact of these molecular assemblies on MOF particle formation. Ultimately, therefore, charting MOF nucleation demands an in-depth characterization across different length scales to unite the somewhat different "worlds" of metal-organic ligand assembly and MOF crystallization.

Herein, we present an *in situ* characterization approach probing the molecular-scale assembly processes of MOF materials, while simultaneously studying the nucleation kinetics at the particle level. We combine (1) *in situ* visible (VIS) absorption spectroscopy to speciate the geometry and ligand coordination of metal-organic complexes in solution, (2) ESI-MS to detect oligomeric (pre-)nuclei, and (3) *in situ* elastic scattering in the VIS spectrum to monitor MOF particle formation. This multi-length-scale characterization strategy is complemented by density functional theory (DFT) calculations and molecular dynamics (MD) simulations to unravel the molecular driving forces behind pre-nucleation. The multi-scale characterization approach is exemplified for ZIF-67,[8,24] an archetypal[5] $Co(2\text{-mIm})_2$ zeolitic imidazolate framework (ZIF) with sodalite topology, but is widely applicable to other MOFs and porous frameworks with electronic transitions in the VIS range.

## RESULTS

### Initial formation of a chemically diverse metal-organic linker pool

To gather information on the coordination geometry of Co-complexes in solution, VIS absorption spectra are recorded before and after mixing a 5 mM $Co(NO_3)_2 \cdot 6H_2O$ and 50 mM 2-methylimidazole (2-mIm) methanolic solution (Figure 1B). By placing a filled quartz cuvette in the beam position of the VIS spectrometer setup (Figure 1A), VIS absorption spectra are obtained prior to (Figure 1C, pink) and after (Figure 1C, purple) metal-linker mixing. Prior to mixing, the pale pink $Co(NO_3)_2 \cdot 6H_2O$-methanol solution (Figure 1B) exhibits a low-intensity absorption feature, which is characteristic for $Co^{2+}$ ($3d^7$ $4s^2$) with $Co(OR)_6$-type octahedral ($O_h$) symmetry, with OR originating from $H_2O$ ($OH^-$), $CH_3OH$ ($CH_3O^-$), and/or $NO_3^-$ ligands (Figure 1C, pink; Note S1).[25] Upon mixing, the solution immediately changes color to deep purple caused by an intensity gain and redshift of the peak maximum, typical for $O_h$ to tetrahedral ($T_d$) transitions (absorbance $\approx$0.04 $\rightarrow$ 0.55, max $\approx$512 nm $\rightarrow$ 561 nm; Figure 1C, purple; Note S1). The dominant absorption strongly resembles spectra of $T_d$ $Co(Im)_3OH^-$ complexes in biomimetic carbonic anhydrases, consisting of $Co^{2+}$ centers bound to three imidazole end groups of histidine amino acids and one $H_2O$ molecule/$OH^-$ anion (Figure 1C, purple; Note S1).[26–28] Linear combination fitting (LCF) of $Co(OR)_6$, $Co(2\text{-mIm})_3OR$, and $Co(2\text{-mIm})_4$ fingerprints (Figure 1C, orange, light and dark brown, respectively) to the experimental spectrum results in good convergence and confirms the dominant contribution of the $Co(2\text{-mIm})_3OR$ configuration (Note S1; Figures S1–S4). Based on LCF, $O_h$ $Co(OR)_6$-type complexes (e.g., $Co(OR)_6$, $Co(2\text{-mIm})_1(OR)_5$, and $Co(2\text{-mIm})_2(OR)_4$), coexist with $T_d$ $Co(2\text{-mIm})_3OR$ and $Co(2\text{-mIm})_4$ in the solution after mixing. $T_d$ Co-complexes have identical coordination as Co in ZIF-67, which shows three spin-orbit split excitations at 546, 567, and 600 nm (Note S1).[29]

Please cite this article in press as: Filez et al., Elucidation of the pre-nucleation phase directing metal-organic framework formation, Cell Reports Physical Science (2021), https://doi.org/10.1016/j.xcrp.2021.100680





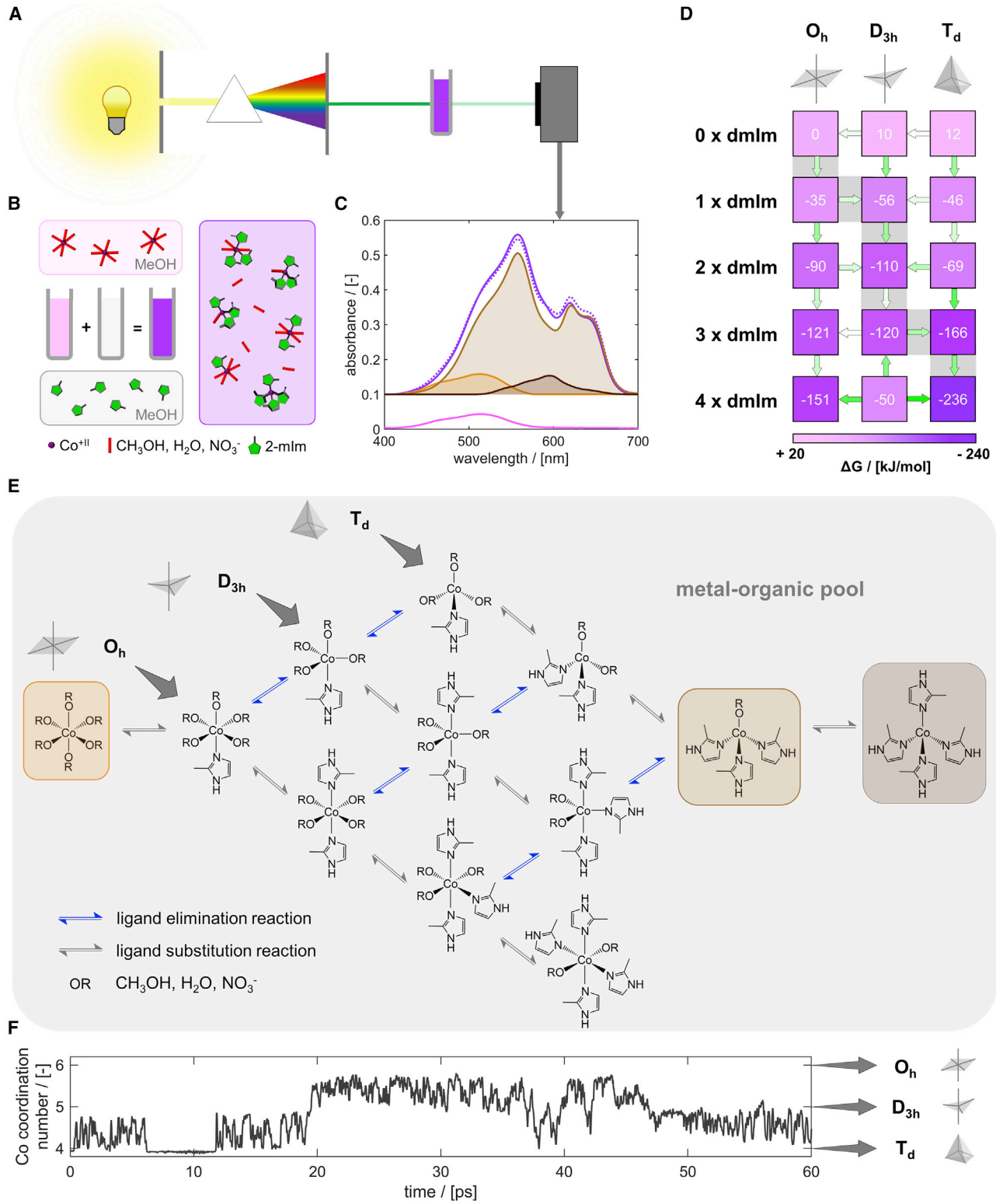


**Figure 1. Formation of metal-organic linker pool by mixing $Co^{2+}$ and 2-mIm solutions**

(A) UV-VIS setup yielding absorption spectra after white beam dispersion (prism) and wavelength selection (slit).

(B) Mixing 5 mM $Co(NO_3)_2 \cdot 6H_2O$ (pink) and 50 mM 2-methylimidazole (2-mIm, transparent) methanolic solutions induces rapid color change (purple) due to ligand substitution/elimination reactions and coordination changes of $Co(OR)_6$ (OR = methanol, $H_2O$, $NO_3^-$) to $Co(2\text{-mIm})_x(OR)_{y-x}$.

Introduction of the 2-mIm organic linker in the $Co(NO_3)_2 \cdot 6H_2O$ solution, thus, triggers rapid ligand exchange and elimination reactions, which result in fast Co-2-mIm coordination and symmetry changes from $O_h \rightarrow T_d$. To understand the determining factors driving these transitions, thermodynamic analysis was performed on a library of Co-complexes with different ligands and symmetries (Note S2; Figure S5; Tables S1–S5). The Gibbs free energies of Co-complex formation ΔG (kJ/mol) at 298 K using an implicit solvation model (Note S2) are presented in Figure 1D for a selected set of stable symmetries ranging from $T_d$ (4-fold), trigonal bipyramidal $D_{3h}$ (5-fold), and $O_h$ (6-fold) with varying numbers of 1,2-dimethylimidazole (1,2-dmIm) ligands. 1,2-dmIm was used instead of 2-mIm to prevent dimerization and to solely study the initial change in Co-symmetry and coordination. The analysis shows that imidazole ligands form stronger ligand bonds compared to the OR ligands as the Gibbs free energy significantly drops for successive introductions of 1,2-dmIm to the $Co^{2+}$ complex (Note S2). However, from more than two 1,2-dmIm substitutions, the steric hindrance prevents further straightforward substitutions, and, thus, a symmetry reduction takes place from $O_h \rightarrow D_{3h} \rightarrow T_d$. This analysis shows two important driving factors for the formation of $T_d$ Co-complexes, namely, the formation of strong imidazole-type coordination bonds and symmetry reduction.

To investigate the temporal stability and evolution of these Co-complexes in their true solvated molecular environment, a series of first principle MD simulations was performed starting from the $Co(1,2\text{-dmIm})_4$ $T_d$ complex in methanol (Note S2; Figures S6–S8), indeed confirming its stability. Additional metadynamics simulations were performed to enforce changes in the Co-coordination number that reveal intermediate states also observed in the thermodynamic analysis (Note S2). Both concerted and stepwise transition states are observed for the exchange between methanol and 1,2-dmIm. A dynamic evolution of the coordination state is observed, with frequent conformational changes of the complexes, especially in $D_{3h}$ geometries (Figure 1F). For these reasons, the reaction can proceed via multiple pathways (Figure 1E) rather than via an isolated single mechanism.

Metal-linker mixing, thus, triggers kinetically fast ligand exchange and elimination reactions leading to 2-mIm-enriched Co-complexes with reduced symmetry compared to initial linker-free $Co(OR)_6$ (Figure 1E). This reaction series evolves toward a pre-equilibrium, which manifests over short time-scales after mixing and precedes the absolute equilibrium—namely, ZIF-67 formation—in accordance with the model of Goodwin et al.[30] Under the pre-equilibrium condition, a chemically diverse metal-organic linker pool is formed in the solution containing $Co(2\text{-mIm})_{4-x}(OR)_{x+y}$ complexes with $O_h$, $D_{3h}$, and $T_d$ geometry and varying 2-mIm linker abundance (x = 0–4, y = 0–2). These Co-complexes act as precursors or pre-nucleation building units (PNBUs[31]) for ZIF nucleation, having coordination intermediate to initial $O_h$ $Co(OR)_6$ and $T_d$ $Co(2\text{-mIm})_4$ in bulk ZIF-67.

## From metal-organic linker pool species to the formation of oligomeric nuclei

To provide information on the initial stages of nucleation, the abundance and speciation of the oligomers formed are extracted from the ESI-MS data collected 2 min

(C) VIS absorption spectra before (pink) and after (purple) $Co(NO_3)_2 \cdot 6H_2O$-2-mIm mixing. A linear combination fit (LCF) (purple, dotted) deconvolutes the spectrum after mixing into $Co(OR)_6$ (orange), $Co(2\text{-mIm})_3(OR)$ (light brown), and $Co(2\text{-mIm})_4$ (dark brown) constituents.

(D) Reaction scheme derived from static DFT showing the Gibbs free energy of Co-complex formation ΔG (kJ/mol) at 298 K for tetrahedral ($T_d$), trigonal bipyramidal ($D_{3h}$), and octahedral ($O_h$) symmetries with varying numbers of dimethylimidazole (dmIm) ligands forming a reaction network connected by green arrows (intensity indicating $\Delta G_f – \Delta G_i$).

(E) Reaction network of ligand elimination and substitution reactions leading to fast pre-equilibrium formation toward a metal-organic pool. $Co(OR)_6$, $Co(2\text{-mIm})_3(OR)$, and $Co(2\text{-mIm})_4$ complexes correspond to orange, light brown, and dark brown spectra used for LCF.

(F) Variability of $Co^{2+}$ coordination number versus time during a metadynamics simulation.

Please cite this article in press as: Filez et al., Elucidation of the pre-nucleation phase directing metal-organic framework formation, Cell Reports Physical Science (2021), https://doi.org/10.1016/j.xcrp.2021.100680





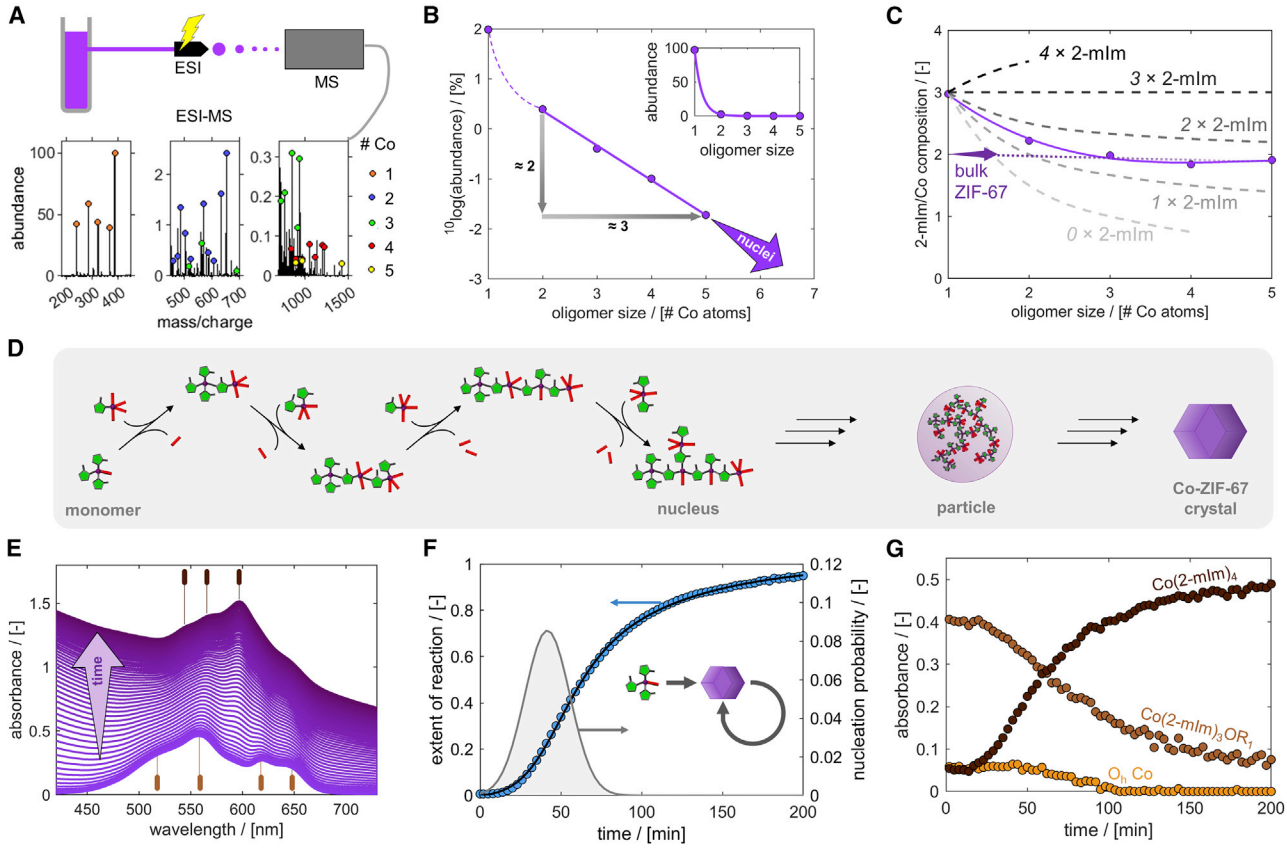


**Figure 2. Formation of oligomeric nuclei and ZIF-67 crystals**

(A) ESI source in which a 5-mM $Co(NO_3)_2.6H_2O$ and 50-mM 2-mIm methanolic mixture is injected, electrosprayed, and projected toward the MS inlet, yielding relative abundances versus mass/charge spectra. Automated peak analysis yields the intensities of $Co_n$ oligomers with size n = 1–5.

(B) The 10-base logaritmic abundance versus oligomer size, derived from ESI-MS in (A). Inset: abundance versus oligomer size.

(C) The 2-mIm/Co-composition as a function of oligomer size (purple) and theoretical ratio evolutions for single-type Co-complex additions with 0–4 × 2-mIm ligands to initial $Co(2\text{-mIm})_3OR$ (dashed gray lines).

(D) Reaction mechanism of oligomerization.

(E) VIS absorption spectra recorded after mixing methanolic 5-mM $Co(NO_3)_2 \cdot 6H_2O$ and 50-mM 2-mIm solutions during ZIF-67 formation (3-min time resolution). Characteristic bands for $Co(2\text{-mIm})_3OR$ (light brown, bottom) and $Co(2\text{-mIm})_4$ (dark brown, top) are indicated.

(F) Absorbance at 400 nm versus time, originating from particle scattering in the VIS background (blue markers). Gualtieri model fit to data (black line) and Gualtieri-derived nucleation probability (gray line, shaded area).

(G) $Co(OR)_6$ (orange), $Co(2\text{-mIm})_3OR$ (light brown), and $Co(2\text{-mIm})_4$ (dark brown) absorbances versus time obtained by LCF to the background subtracted d-d region shown in (E).

after mixing (Figure 2A). ESI-MS peaks down to 0.01% of the maximal peak intensity are identified, linked to their stoichiometric composition, and regrouped according to the detected number of Co-atoms in the complex (Note S3; Figure S9). Figure 2B (inset) shows a steep decrease in the mono- compared to the oligomer abundances, implying that oligomeric species are comparatively rare to monomeric units. Particularly, a base-10 logarithmic plot specifies that (1) the dimer concentration is 1.5 orders of magnitude lower compared to the monomeric abundance, and (2) the oligomer concentration decays exponentially as a function of the oligomer size with order 2/3, leading to a 100-fold concentration decrease from di- to pentamers.

A question of interest remains whether nuclei form via monomeric additions to an oligomer or by oligomer-to-oligomer attachment. Here, the latter is statistically improbable compared to monomer-to-oligomer reactions: the monomer excess in

solution compared to oligomers results in a >1.5 orders of magnitude higher probability for nucleation by monomer-to-oligomer attachment. The formation of stable nuclei is, thus, expected to occur via the progressive incorporation of monomeric units into the oligomeric assemblies, initially following a chain-growth-type polymerization mechanism. Subsequently, these oligomers gradually evolve into stable nuclei, likely with decaying abundance (Figure 2B, arrow), and grow into a certain number of crystals per volume solution mixture.

To further speciate the monomer-to-oligomer reaction mechanism, the oligomer composition is plotted as the 2-mIm/Co-ratio versus the oligomer size (Figure 2C). In addition, dashed curves show the simulated 2-mIm/Co-evolutions when Co-monomers with n × 2-mIm linkers (n = 0–4) are repetitively added to initial Co(2-mIm)$_3$OR (Note S4; Figures S10 and S11). For monomeric Co$_1$-complexes, three methylimidazole ligands coordinate Co, on average, in accordance with the dominant Co(2-mIm)$_3$OR contribution in VIS. Upon oligomerization (Co$_{2\text{-}5}$) the 2-mIm/Co-ratio decreases intermediate to the evolutions of model Co-monomer additions with 1 × 2-mIm and 2 × 2-mIm linkers, eventually stabilizing ≈2 at the bulk Co(2-mIm)$_2$ stoichiometry of ZIF-67. A reaction mechanism involving alternating attachments of Co-monomer with 1 × 2-mIm and 2 × 2-mIm linkers to initial Co(2-mIm)$_3$OR can thus—on average—describe the observed oligomerization process (Figure 2D).

In the initial steps of nucleation, the initial Co(2-mIm)$_3$OR complex, thus, oligomerizes by accommodating 2-mIm-poor monomeric complexes until reaching the ZIF-67 2-mIm/Co ≈ 2 ratio. This finding is in line with atomic force microscopy (AFM) observations indicating ZIF growth via monomeric 2-mIm-poor complex additions.[22,32] A driving factor behind this observation could be the higher configurational probability of initial Co(2-mIm)$_3$OR to react with 2-mIm-poor compared to 2-mIm-rich monomers. Once reaching the bulk 2-mIm/Co-ratio, the oligomer forms a stable nucleus that can grow into ZIF-67 by keeping its 2-mIm/Co-ratio constant (e.g., by continued monomer [1] addition (Note S4; Figures S12 and S13), [2] substitution [healing], and/or [3] nucleus restructuring into gels, nets, and [semi-]crystalline frameworks).[33]

Several nucleation theories can describe MOF nucleation[5,18,34] by gaining inspiration from zeolites[35–37] and other materials[38,39]: (1) (semi-)amorphous gel formation followed by growth and restructuring in crystals, (2) formation of PNBUs that directly assemble into crystals, and (3) oriented particle-to-particle attachment of crystalline nanosized MOF entities. Nucleation of ZIFs, including ZIF-8/ZIF-67, was suggested to occur via (semi-)amorphous gel formation, preceding crystallization. Particularly, PDF suggests ~2 nm amorphous ZIF particles being formed in solution,[20] while TEM[40,41] and SAXS-WAXS[12] show (semi-)amorphous ZIF particles during nucleation. Our observations can pinpoint the underlying molecular reasons of (semi-)amorphous particle formation. The metal-organic pool contains a distribution of Co-complexes with high geometric and compositional variability ($O_h$, $D_{3h}$, $T_d$; 0–4 × 2-mIm linkers). When participating in monomer-to-oligomer additions, Co-monomers with strongly differing coordination states attach to oligomeric (pre-)nuclei. Indeed, ESI-MS shows that 2-mIm-poor Co-complexes add to the (pre-)nucleus, while DFT clears out that these 2-mIm-poor complexes disfavor $T_d$ geometry. This likely results in particles with configurationally disordered thermoset-type polymers, exhibiting (semi-)amorphicity.

In contrast, nucleation by direct assembly of PNBUs into ZIF crystals is not suggested. The latter requires single-type PNBUs with direct geometric and

compositional resemblance to the crystal constituents—for example, $T_d$ Co(2-mIm)$_2$(OR)$_2$ (2-mIm/Co = 2). The metal-organic pool, however, contains diverse complexes with geometries and compositions very different from bulk coordination. This hinders straightforward assembly into crystalline ZIFs, unlike nucleation of non-zeolitic MOFs including UiO-66,[19] MOF-5/2,[42] MIL-89/101,[43,44] and others.[45]

### From oligomeric nuclei to ZIF-67 formation

*In situ* VIS spectra are recorded with 3 min time resolution immediately after mixing methanolic 5 mM $Co(NO_3)_2 \cdot 6H_2O$ and 50 mM 2-mIm solutions (pre-equilibrium state) until ZIF-67 is formed (Figure 2E). The VIS background increase originates from elastic Rayleigh/Mie scattering of (pre-)ZIF-67 particles and is characteristic for macroscopic particle formation, leading to a turbid non-transparent solution. When monitored at 400 nm, the background displays archetypal sigmoidal Avrami-Erofeev[46] nucleation and growth behavior (Figure 2F; Note S5). Fitting a Gualtieri model[47] to this curve (Figure 2F, black curve) yields excellent convergence and provides the probability distributions of nucleation (Figure 2F, gray zone). The crystallization process stabilizes after 150 min.

Considering both the scattering background and the electronic $Co^{2+}$ d-d transitions in the absorption spectrum allows us to correlate the molecular Co-ligand complex changes, which accompany macroscopic ZIF-67 crystal formation. VIS inspection of the d-d region (450–700 nm) in the absorption spectrum shows that the background increase is accompanied by a Co(2-mIm)$_3$OR → Co(2-mIm)$_4$ transition. LCF of the time-resolved spectra using Co(OR)$_6$, Co(2-mIm)$_3$OR, and Co(2-mIm)$_4$ fingerprints reveals the kinetics of Co-complex consumption/production (Figure 2G). $O_h$ Co- and Co(2-mIm)$_3$OR-type complexes are consumed to form Co(2-mIm)$_4$, characteristic for ZIF-67. The intensity profiles follow the same dynamics as the particle scattering background (Figure 2F), showing that particle formation and Co-complex consumption are intimately related. An autocatalytic kinetic model is applied to simulate the VIS Co-complex consumption and production rates and yields excellent convergence (Note S5; Figure S14).

### Molecular criteria for nucleation of zeolitic imidazolate frameworks

The combined *in situ* VIS/ESI-MS methodology is now applied to a broad range of organic linker/metal (*L*/*M*) ratios, allowing to assess when macroscopic particle formation takes place and determine the underlying molecular criteria (*L*/*M* = 1–40, [$Co(NO_3)_2.6H_2O$] = 5 mM). On the macroscopic scale, sigmoidal Avrami-Erofeev-type curves are obtained from the *in situ* VIS background (400 nm) for *L*/*M* ranging from 4 to 40, while no nucleation is observed for *L*/*M* = 3 and below (Figure 3B). With increasing *L*/*M* from 4 to 15, the nucleation delay decreases, and particle formation is more extensive (arrow, top left), while *L*/*M* of 15–40 suggests a stagnation of the nucleation rates with possible gentle decrease (arrow, right). Analogous to VIS background fitting in Figure 2F, the Gualtieri model is repetitively applied for *L*/*M* ranging from 4 to 40. This yields the Gualtieri-derived nucleation rates (Figure 3C), quantitatively describing the trends observed in the *in situ* VIS backgrounds (Figure 3B).

At the molecular scale, VIS spectra recorded 2 min after metal-linker mixing for *L*/*M* = 1–40 contain information on the coordination of Co-complexes in solution (Figure 3F). With increasing *L*/*M* ratio, VIS spectra display peak shifts and appearances evolving from $O_h$ Co to $T_d$ Co(2-mIm)$_3$OR and $T_d$ Co(2-mIm)$_4$. VIS-LCF analysis (Figure 3G; Note S1) yields $T_d$ Co(2-mIm)$_3$OR, $T_d$ Co(2-mIm)$_4$ and $O_h$ Co-spectral contributions for *L*/*M* = 1–40. In accordance with the Le Châtelier principle, the

Please cite this article in press as: Filez et al., Elucidation of the pre-nucleation phase directing metal-organic framework formation, Cell Reports Physical Science (2021), https://doi.org/10.1016/j.xcrp.2021.100680



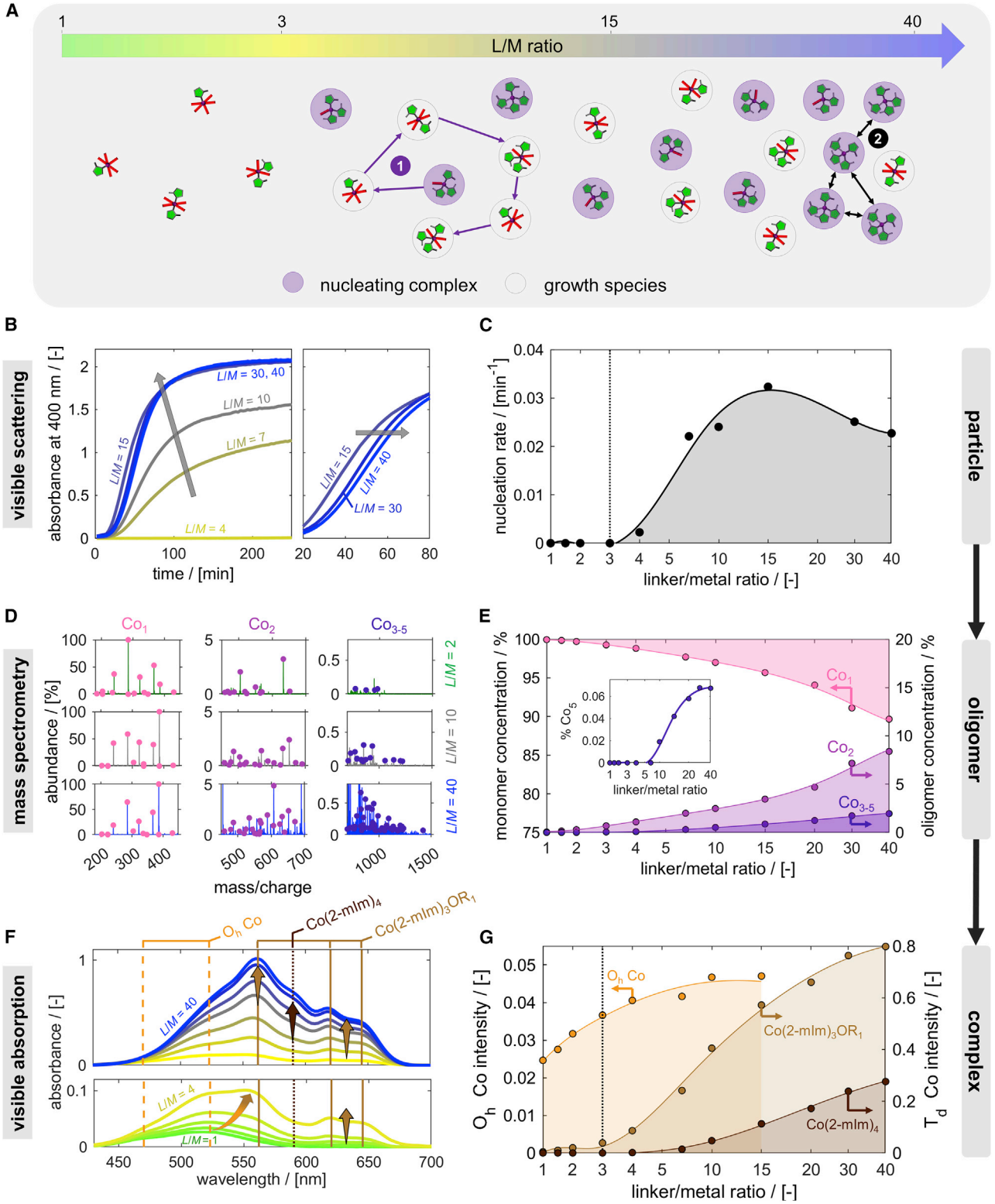


**Figure 3. Linking molecular pre-equilibrium composition to macroscopic nucleation rates**

(A) Schematic representation of pre-equilibrium state with increasing linker/metal ratios (*L/M*) extracted from ESI-MS and VIS. Events are indicated: (1) oligomerization initiated by a nucleating complex with growth species and (2) repulsion of $T_d$ $Co(2\text{-mIm})_4$ nucleating complexes.

metal-organic linker pool composition shifts to more 2-mIm-rich Co-complexes with increasing *L/M* ratio (Figures 3A and 1E, reaction scheme). Particularly, with increasing *L/M* ratio, the $O_h$ Co-intensity increases due to increased Co-2-mIm coordination, leading to steric distortion of the $O_h$ symmetry. From *L/M* = 4 onward, a non-negligible population of $T_d$ $Co(2\text{-mIm})_3OR$ and $Co(2\text{-mIm})_4$ complexes appears. Nucleation and particle formation at a macroscopic level ($L/M \geq 4$), thus, requires $T_d$ $Co(2\text{-mIm})_3OR$ and/or $Co(2\text{-mIm})_4$ complexes in the metal-organic pool (Figure 3A[1]).

This finding is supported by ESI-MS, which provides the abundances of $Co_n$ oligomers for different *L/M* ratios via mass spectra. Particularly, the number of detected $Co_2$ and $Co_{3-5}$ oligomer peaks and their normalized abundances increase from *L/M* = 2 to 10 to 40 (Figure 3D). Increasing the *L/M* ratio, thus, has a strong influence on the abundance of oligomers formed. Systematic analysis over the full *L/M* range shows a progressive increase in the number of Co-oligomers, while stable $Co_{3-5}$ nuclei are quasi-absent for $L/M \leq 3$ (Figure 3E). For $L/M \leq 3$, the lack of $T_d$ $Co(2\text{-mIm})_3OR$ and/or $Co(2\text{-mIm})_4$ molecular complexes in the metal-organic pool, thus, inhibits $Co_{3-5}$ nucleus formation and subsequent macroscopic particle formation.

At high *L/M* ratios (>15), the $Co(2\text{-mIm})_3OR$ intensity seems to stabilize, while the $Co(2\text{-mIm})_4$ complex contribution progressively intensifies. Such higher $Co(2\text{-mIm})_4$ abundances might induce $Co(2\text{-mIm})_4$-$Co(2\text{-mIm})_4$ repulsions (Figure 3A[2]), which start hindering nucleus and particle formation due to their mutual bridging inabilities, in accordance with the work of Domke et al.[48] Indeed, the $Co_5$ nucleus abundance (Figure 3E, inset) stabilizes for high *L/M* ratios, showing strong correlation to stabilized macroscopic nucleation rates (Figure 3C).

Metal-organic complexes in the pool can, thus, be classified in two groups (Figure 3A): (1) nucleating complexes and (2) growth species that add to the nucleating complexes, oligomers, and nuclei to yield ZIFs. Nucleating complexes resemble the final $Co(2\text{-mIm})_4$ geometry in ZIF-67, (i.e., $Co(2\text{-mIm})_3OR$ and $Co(2\text{-mIm})_4$) and are responsible for initiating oligomerization. Growth species include nucleation complexes but also contain more chemically diverse complexes with different symmetry and lower 2-mIm linker coordination (e.g., $O_h$, $D_{3h}$, and $T_d$ Co-complexes with 0–4 × 2-mIm).

## Toward molecular synthesis control

In Figure 4A, a fundamental relationship is described between (input) the organic linker/metal *L/M* ratio and (output) the size and density of ZIF-67 crystals by linking these macroscopic parameters to the molecular abundances of (1) $T_d$-type "nucleating complexes" and (2) $Co_{3-5}$ oligomeric nuclei. Figure 4A displays four subgraphs that are interlinked: (top left) linker/metal ratio (synthesis) versus $T_d$ Co-complex intensity (VIS-LCF), (bottom left) abundance of $Co_{3-5}$ oligomeric nuclei (ESI-MS)

(B) Absorbance at 400 nm versus time, originating from particle scattering in the VIS background, for a series of *L/M* for 5-mM $Co(NO_3)_2.6H_2O$-methanol and *L/M* × 5-mM 2-mIm-methanol solutions.
(C) Nucleation rates versus *L/M* derived from Gualtieri model fitting the S-shaped curves in (B).
(D) ESI-MS profiles for *L/M* = 2 (green), 10 (gray), and 40 (blue). Peaks corresponding to $Co_1$ (pink), $Co_2$ (light purple), and $Co_{3-5}$ (purple) oligomers are indicated.
(E) Relative fraction of monomer ($Co_1$, pink), dimer ($Co_2$, light purple), and $Co_{3-5}$ (purple) oligomers as a function of *L/M* ratio. The inset displays the $Co_5$ nuclei fraction.
(F) VIS absorption spectra for *L/M* = 1–40 (green-yellow-gray-blue) immediately after mixing and peak positions for $O_h$ Co (orange), $Co(2\text{-mIm})_3OR_1$ (light brown), and $Co(2\text{-mIm})_4$ (dark brown).
(G) $O_h$ and $T_d$ peak intensities versus *L/M* after LCF. $O_h$ intensities can be reliably estimated only for *L/M* = 1–15 due to their relatively low intensities.

Please cite this article in press as: Filez et al., Elucidation of the pre-nucleation phase directing metal-organic framework formation, Cell Reports Physical Science (2021), https://doi.org/10.1016/j.xcrp.2021.100680



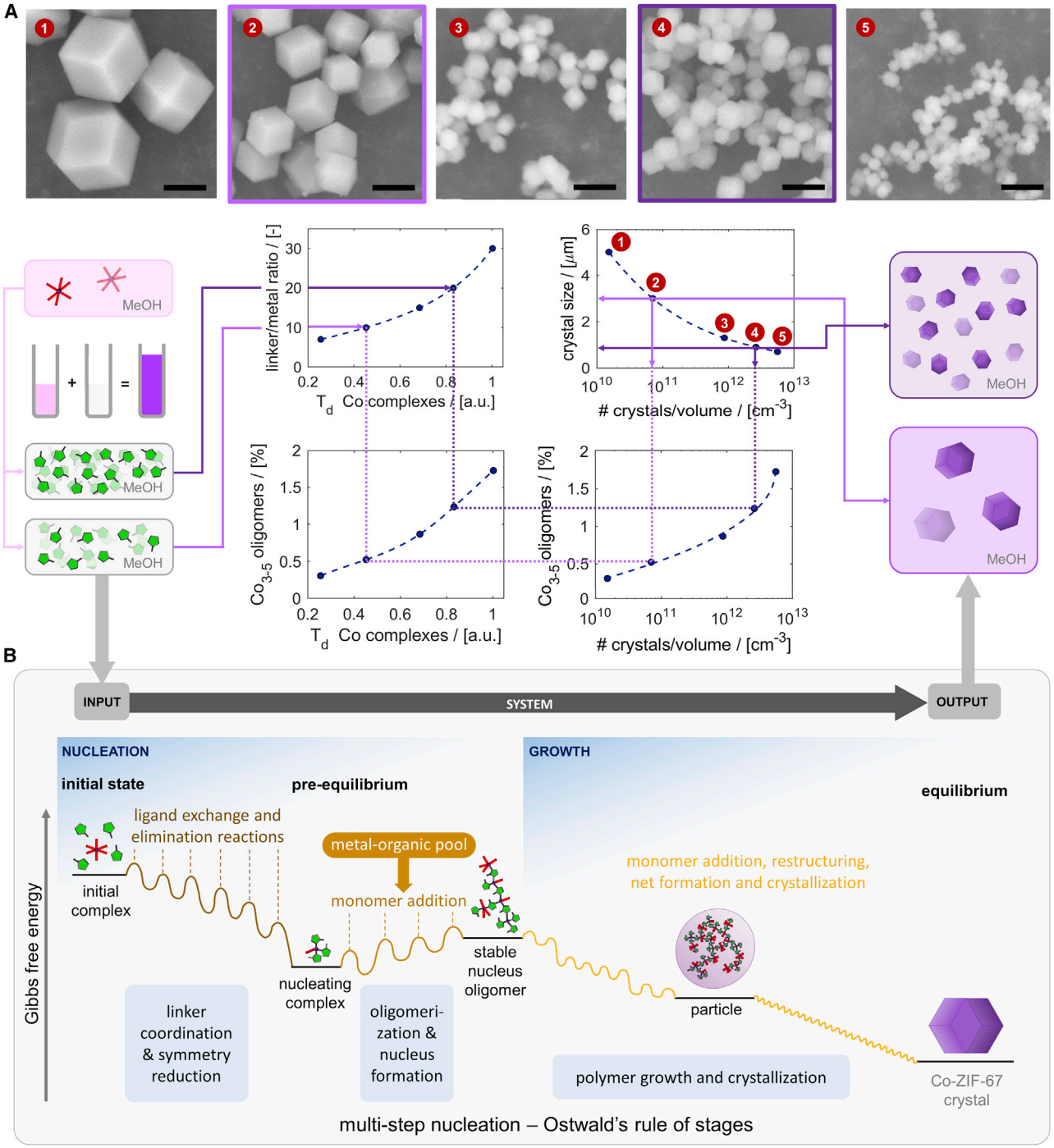


**Figure 4. Molecular nucleation pathways linking macroscopic input (*L/M*) to macroscopic output (crystal size and density) parameters**

(A) Schematic illustration of one metal and two linker solutions with different concentrations, yielding two *L/M* input conditions for ZIF synthesis (light purple and purple lines). These input conditions lead to output ZIF crystals with specific size and number density (Note S6; Figure S15). The macroscopic input-output relationship is governed by metal-organic reaction species on the microscopic level, namely, (1) nucleating complexes (i.e., $T_d$ Co-complexes with 3–4 × 2-mIm linkers that trigger nucleation), yielding a specific number of (2) stable $Co_{3-5}$ oligomeric nuclei. Scanning electron microscopy (SEM) images show the crystal sizes for different *L/M* ratios. Scale bar: 2.5 μm.

(B) Schematic overview of the molecular nucleation pathway from metal-linker mixing to crystal product formation (input-output), containing different stages (i.e., nucleation and growth) and states: (1) initial, (2) pre-equilibrium (metal-organic pool), and (3) equilibrium (ZIF-67).

versus $T_d$ Co-complex intensity (VIS-LCF), (bottom right) abundance of $Co_{3–5}$ oligomeric nuclei (ESI-MS) versus the number of crystals/volume (density, scanning electron microscopy (SEM), and product yield), and (top right) crystal size (SEM, images at the top of Figure 4A) versus the number of crystals/volume (SEM and product yield). The light and dark purple lines represent low and high *L*/*M* ratio mixtures, respectively, and run through the sub-graphs. The *L*/*M* synthesis parameter forms a powerful handle to steer the metal-organic pool composition toward the desired concentration of nucleating complexes, on its turn influencing the $Co_{3–5}$ nucleus concentration and number and size of crystals formed. Particularly, high *L*/*M* ratios force 2-mIm linkers to increasingly coordinate metal-organic pool complexes according to the Le Châtelier principle and shift the pre-equilibrium to the right-hand side of the reaction network in Figure 1D. This generates more oligomeric nuclei, which grow into crystals of reduced size. This molecular image is consistent with a more classic picture of competition between crystal nucleation and growth at high supersaturation favoring the former.

## DISCUSSION

We have speciated the molecular origins of $Co(2\text{-mIm})_2$ ZIF-67 nucleation, thereby clarifying non-classic nucleation pathways (Figure 4B). Upon initial Co-2-mIm mixing, original metal-organic complexes undergo a cascade of linker exchange and elimination reactions, leading to rapid metal-linker coordination and symmetry reduction (theory). This generates a chemically diverse pool of metal-organic linker complexes with broad geometric and compositional variability, ranging from $O_h$ to $T_d$ Co with 0–4 × 2-mIm linkers (VIS). This pool serves as a reservoir for nucleation into ZIF-67 and forms a pre-equilibrium state preceding ZIF-67 crystallization. Within the metal-organic pool, we identify (1) "nucleation complexes" or 2-mIm-rich $T_d$ Co-complexes isostructural to Co in ZIF-67, and (2) "growth species," more 2-mIm-poor Co-complexes with diverse $O_h$, $D_{3h}$, or $T_d$ symmetry. Nucleation complexes are required to start oligomerization into stable nuclei, occurring by repetitive addition of monomeric growth units (ESI-MS). The geometric diversity of these growth species can cause structural disorder and clarifies the (semi-)amorphous nature of particles reported in the early stages of ZIF nucleation, as well as their multi-step nucleation pathway. The long-debated relationship between the linker-to-metal ratio during synthesis (input) and the crystal product size and number (output) is elucidated by insights in the molecular pre-equilibria of the metal-organic pool and its consequences on nucleation (SEM, VIS, ESI-MS). While the kinetics and thermodynamics of MOF formation are dependent on the metal-linker combination and synthesis conditions, we show the direct impact of metal-organic reaction chemistries on the pathways that direct framework formation. For other MOFs, the presence of a chemically diverse metal-organic pool is expected to be more rule than exception, given the multi-step nature of ligand exchange and elimination reactions from linker-free complexes into their final MOF coordinations. Such complexity likely introduces non-classic multi-stage nucleation routes that are dictated by the chemistries of the MOF's coordination metal.

## EXPERIMENTAL PROCEDURES

### Resource availability

#### *Lead contact*

Further information and requests for resources and reagents should be directed to and will be fulfilled by the lead contact, Bert M. Weckhuysen (b.m.weckhuysen@uu.nl).

#### *Materials availability*

This study did not generate new unique reagents.

### Data and code availability

All other data and code supporting the findings of this study are available within the article and are described in the Supplemental information or are available from the corresponding author upon reasonable request.

## Method details

### ZIF-67 synthesis

The 5-mM $Co(NO_3)_2.6H_2O$–methanol solutions were prepared by dissolving 0.1455 g $Co(NO_3)_2.6H_2O$ (99% Sigma-Aldrich) in 100 mL methanol (99.99% Sigma-Aldrich). The 2-methylimidazole-methanol solutions with 5, 7.5, 10, 15, 20, 35, 50, 75, 100, 150, and 200 mM concentrations were prepared by adding 1.642 g 2-methylimidazole (2-mIm, 99%, Sigma-Aldrich) to 100 mL methanol (99.99% Sigma-Aldrich), yielding a 200-mM 2-mIm–methanol solution and subsequent dilution into the listed concentrations. To initiate ZIF-67 nucleation, 2 mL of a 2-mIm solution is mixed with a 2 mL Co-precursor solution. Subsequently, the 2-mL 2-mIm solution is directly added to the 2-mL Co-precursor solution by mixing two vial volumes in 1 s. Immediately after adding the 2-mIm solution to the Co-precursor solutions, the 4-mL Co-2-mIm mixture is shaken eight times during 4 s. No stirring or sonication is applied to prevent influence on the nucleation and growth process. Bulk characterization by X-ray diffraction, thermogravimetric analysis, $N_2$ physisorption, and Raman spectroscopy is provided in Note S7 and Figures S16–S20 for all products, evidencing that ZIF-67 is formed, while scanning electron microscopy images are shown in Figure 4A.

### UV-VIS spectroscopy

UV-VIS spectra were recorded from 250 to 850 nm using a Lambda 950 S spectrophotometer with tungsten-halogen (>319 nm) and deuterium (<319 nm) lamps (Perkin-Elmer). Prior to measurement, 0% and 100% transmission spectra were collected for data correction. A 4-mL Co-2-mIm mixture is added to a quartz cuvette of the same volume with 1 cm beam path length. In addition, an identical quartz cuvette is filled with the pure solvent. Both cuvettes are placed in the UV-VIS spectrometer beam path for transmission measurement using a split beam that irradiates both cuvettes containing the Co-2-mIm mixture and pure solvent, the latter used for background subtraction. UV-VIS data collection with 3 min temporal resolution is initiated 120 s after Co-2-mIm mixing (spectral resolution 2.5 nm). The quartz cuvettes were cleaned using hydrochloric acid (36%) after measurement to prevent heterogeneous ZIF-67 nucleation on ZIF-contaminated cuvette surfaces.

### ESI-MS

Spectra were recorded on a Q-Exactive Orbitrap (Thermo Fisher Scientific, Bremen, Germany) in positive ion mode. Samples were electrosprayed using a syringe pump at a flow of 5 μl/min coupled to an Ion Max Source set to 3.4-kV spray voltage. A mass range of 150–2000 m/z was used with a resolving power of 140,000 at m/z 200 and an AGC target of $1 \times 10^6$. For each sample, 50 scans were acquired with 10 μ scans per scan. After each sample, a reference of pure methanol was acquired for data correction. Between each experiment, the syringe used for electrospray was washed several times to minimize carryover.

### DFT, MD, and metadynamics

Static DFTs are employed to assess the structure and stability of $Co(dmIm)_m(CH_3OH)_n$ complexes ($4 \leq m+n \leq 6$, $0 \leq m \leq 4$, $0 \leq n \leq 6$). 1,2-dmIm is used to reduce computational complexity regarding (de-)protonation equilibria of the non-bound pyrrole-type N-H in 2-mIm by substituting the H with a $CH_3$ group. The

5-coordinated square pyramidal ($C_{4v}$) $Co^{2+}$ complexes are not considered since, in general, they show low spin ($S = 1/2$), which would require a double-spin crossover from $S = 3/2$ ($O_h$) → $1/2$ ($C_{4v}$) → $3/2$ ($T_d$) being highly unlikely. Moreover, these geometries are not observed in the MD simulations. Furthermore, the first ligand removal in $O_h$ configuration is likely taking place from an equatorial position ($O_h \rightarrow D_{3h}$) due to steric hindrance rather than an axial position ($O_h \rightarrow C_{4v}$). Calculations are carried out with Gaussian 16[49] software, adopting the PBE0 hybrid exchange-correlation functional in conjunction with the 6-31++G(d,p) basis set. The polarizable continuum model scheme is used to simulate the effects of the methanol solvent, and Grimme's scheme reproduced dispersion effects. Various models of the complexes have been set up to mimic the passage from octahedral to tetrahedral compounds. Their relaxed geometries and thermodynamic stabilities are reported in Note S2, while cartesian coordinates of metal-organic complexes are reported in the Data S1 library.

MD and enhanced MD simulations at 298 K have been performed using CP2K[50] and PLUMED[51] on a 15 × 15 × 15 $Å^3$ cubic unit cell, containing the relaxed $T_d$ complex $Co(dmIm)_4^{2+}$ and 52 explicit MeOH molecules. A hybrid Gaussian-planewave basis set was used in an open-shell approach at the PBE-D3 level of theory, with DVZP-GTH basis set and pseudopotentials for the elements except Co, for which DZVP-MOLOPT-GTH was used. The cutoff for the plane waves was set at 400 Ry. The rest of the simulations were performed in the NVT ensemble with a time step of 0.5 fs. A Nosé-Hoover thermostat was used, with a time constant of 0.3 ps and five beads. The simulations were first equilibrated in the NpT ensemble, where the unit cell volume was optimized using a MTK barostat with a time constant of 0.1 ps. To investigate the coordination changes in the complex, two independent metadynamics simulations have been performed, starting from the equilibrated MD run. Gaussian hills have been added every 50 simulation steps along the chosen collective variables, and the evolution of the system has been monitored.

## SUPPLEMENTAL INFORMATION

Supplemental information can be found online at https://doi.org/10.1016/j.xcrp.2021.100680.

## ACKNOWLEDGMENTS

The authors acknowledge Dr. A.D. Chowdhury and Dr. Z. Ozturk for their valuable input and discussions. M.F. acknowledges the European Union's Horizon 2020 research and innovation program under the Marie Sklodowska-Curie grant agreement 748563. B.M.W. acknowledges funding from a European Research Council (ERC) Advanced Grant (321140) as well as the Netherlands Organization for Scientific Research (NWO) in the frame of a Gravitation Program MCEC (Netherlands Center for Multiscale Catalytic Energy Conversion, https://www.mcec-researchcenter.nl). C.C., F.M.-M., and V.V.S. acknowledge funding from the European Research Council under the ERC grant agreement 240483 and the European Union's Horizon 2020 research and innovation program (Consolidator ERC grant agreement 647755 – DYNPOR) and the Research Board of the Ghent University. Computational resources and services were provided by the VSC (Flemish Supercomputer Center), funded by the Research Foundation Flanders (FWO) and the Flemish Government, department EWI. M.F. gratefully acknowledges his parents, wife, and children for their persistent support.

## AUTHOR CONTRIBUTIONS

M.F. and M.R.-T. prepared and characterized samples. M.F. performed VIS experiments. M.F. and M.H. performed ESI-MS experiments, supervised by A.J.R.H.

M.F. performed data analysis of VIS and ESI-MS data and stochastic simulations. F.M.-M. performed static DFT, and C.C. performed MD and MTD simulations under supervision of V.V.S. M.F. and B.M.W. conceived the research idea and managed the project. All authors discussed the results and commented on the different versions of the manuscript.

## DECLARATION OF INTERESTS

The authors declare no competing interests.

Received: June 18, 2021
Revised: September 11, 2021
Accepted: November 15, 2021
Published: December 6, 2021

## REFERENCES

1. Furukawa, H., Cordova, K.E., O'Keeffe, M., and Yaghi, O.M. (2013). The chemistry and applications of metal-organic frameworks. Science *341*, 1230444.

2. Denny, M.S., Moreton, J.C., Benz, L., and Cohen, S.M. (2016). Metal–organic frameworks for membrane-based separations. Nat. Rev. Mater. *1*, 16078.

3. Zhang, X., Huang, Z., Ferrandon, M., Yang, D., Robison, L., Li, P., Wang, T.C., Delferro, M., and Farha, O.K. (2018). Catalytic chemoselective functionalization of methane in a metal–organic framework. Nat. Catal. *1*, 356–362.

4. Stock, N., and Biswas, S. (2012). Synthesis of metal-organic frameworks (MOFs): routes to various MOF topologies, morphologies, and composites. Chem. Rev. *112*, 933–969.

5. Van Vleet, M.J., Weng, T., Li, X., and Schmidt, J.R. (2018). In Situ, Time-Resolved, and Mechanistic Studies of Metal-Organic Framework Nucleation and Growth. Chem. Rev. *118*, 3681–3721.

6. Peters, A.W., Howarth, A.J., and Farha, O.K. (2017). Experimentalists and theorists need to talk. Nature *551*, 433–434.

7. Moosavi, S.M., Chidambaram, A., Talirz, L., Haranczyk, M., Stylianou, K.C., and Smit, B. (2019). Capturing chemical intuition in synthesis of metal-organic frameworks. Nat. Commun. *10*, 539.

8. Banerjee, R., Phan, A., Wang, B., Knobler, C., Furukawa, H., O'Keeffe, M., and Yaghi, O.M. (2008). High-throughput synthesis of zeolitic imidazolate frameworks and application to CO2 capture. Science *319*, 939–943.

9. Wilmer, C.E., Leaf, M., Lee, C.Y., Farha, O.K., Hauser, B.G., Hupp, J.T., and Snurr, R.Q. (2011). Large-scale screening of hypothetical metal-organic frameworks. Nat. Chem. *4*, 83–89.

10. Yaghi, O.M., O'Keeffe, M., Ockwig, N.W., Chae, H.K., Eddaoudi, M., and Kim, J. (2003). Reticular synthesis and the design of new materials. Nature *423*, 705–714.

11. Stavitski, E., Goesten, M., Juan-Alcañiz, J., Martinez-Joaristi, A., Serra-Crespo, P., Petukhov, A.V., Gascon, J., and Kapteijn, F. (2011). Kinetic control of metal-organic framework crystallization investigated by time-resolved in situ X-ray scattering. Angew. Chem. Int. Ed. Engl. *50*, 9624–9628.

12. Cravillon, J., Schröder, C.A., Nayuk, R., Gummel, J., Huber, K., and Wiebcke, M. (2011). Fast nucleation and growth of ZIF-8 nanocrystals monitored by time-resolved in situ small-angle and wide-angle X-ray scattering. Angew. Chem. Int. Ed. Engl. *50*, 8067–8071.

13. Millange, F., Medina, M.I., Guillou, N., Férey, G., Golden, K.M., and Walton, R.I. (2010). Time-resolved in situ diffraction study of the solvothermal crystallization of some prototypical metal-organic frameworks. Angew. Chem. Int. Ed. Engl. *49*, 763–766.

14. Yeung, H.H.-M., Wu, Y., Henke, S., Cheetham, A.K., O'Hare, D., and Walton, R.I. (2016). In Situ Observation of Successive Crystallizations and Metastable Intermediates in the Formation of Metal-Organic Frameworks. Angew. Chem. Int. Ed. Engl. *55*, 2012–2016.

15. Cravillon, J., Nayuk, R., Springer, S., Feldhoff, A., Huber, K., and Wiebcke, M. (2011). Controlling Zeolitic Imidazolate Framework Nano- and Microcrystal Formation: Insight into Crystal Growth by Time-Resolved In Situ Static Light Scattering. Chem. Mater. *23*, 2130–2141.

16. Van Cleuvenbergen, S., Smith, Z.J., Deschaume, O., Bartic, C., Wachsmann-Hogiu, S., Verbiest, T., and van der Veen, M.A. (2018). Morphology and structure of ZIF-8 during crystallisation measured by dynamic angle-resolved second harmonic scattering. Nat. Commun. *9*, 3418.

17. Patterson, J.P., Abellan, P., Denny, M.S., Jr., Park, C., Browning, N.D., Cohen, S.M., Evans, J.E., and Gianneschi, N.C. (2015). Observing the growth of metal-organic frameworks by in situ liquid cell transmission electron microscopy. J. Am. Chem. Soc. *137*, 7322–7328.

18. Rimer, J.D., and Tsapatsis, M. (2016). Nucleation of open framework materials: Navigating the voids. MRS Bull. *41*, 393–398.

19. Xu, H., Sommer, S., Broge, N.L.N., Gao, J., and Iversen, B.B. (2019). The Chemistry of Nucleation: In Situ Pair Distribution Function Analysis of Secondary Building Units During UiO-66 MOF Formation. Chem. Eur. J. *25*, 2051–2058.

20. Terban, M.W., Banerjee, D., Ghose, S., Medasani, B., Shukla, A., Legg, B.A., Zhou, Y., Zhu, Z., Sushko, M.L., De Yoreo, J.J., et al. (2018). Early stage structural development of prototypical zeolitic imidazolate framework (ZIF) in solution. Nanoscale *10*, 4291–4300.

21. Lim, I.H., Schrader, W., and Schüth, F. (2015). Insights into the Molecular Assembly of Zeolitic Imidazolate Frameworks by ESI-MS. Chem. Mater. *27*, 3088–3095.

22. Wagia, R., Strashnov, I., Anderson, M.W., and Attfield, M.P. (2018). Insight and Control of the Crystal Growth of Zeolitic Imidazolate Framework ZIF-67 by Atomic Force Microscopy and Mass Spectrometry. Cryst. Growth Des. *18*, 695–700.

23. Haouas, M., Volkringer, C., Loiseau, T., Férey, G., and Taulelle, F. (2012). In Situ NMR, Ex Situ XRD and SEM Study of the Hydrothermal Crystallization of Nanoporous Aluminum Trimesates MIL-96, MIL-100, and MIL-110. Chem. Mater. *24*, 2462–2471.

24. Phan, A., Doonan, C.J., Uribe-Romo, F.J., Knobler, C.B., O'Keeffe, M., and Yaghi, O.M. (2010). Synthesis, structure, and carbon dioxide capture properties of zeolitic imidazolate frameworks. Acc. Chem. Res. *43*, 58–67.

25. Brozek, C.K., Michaelis, V.K., Ong, T.C., Bellarosa, L., López, N., Griffin, R.G., and Dincă, M. (2015). Dynamic DMF Binding in MOF-5 Enables the Formation of Metastable Cobalt-Substituted MOF-5 Analogues. ACS Cent. Sci. *1*, 252–260.

26. Bauer, R., Limkilde, P., and Johansen, J. (1977). Metal Coordination Geometry and Mode of Action of Carbonic-Anhydrase - Effect of Imidazole on Spectral Properties of Co(ii) and Cd-111(ii) Human Carbonic Anhydrase-B. Carlsberg Res. Commun. *42*, 325–339.

27. Cockle, S.A., Lindskog, S., and Grell, E. (1974). Electron-paramagnetic-resonance studies on cobalt(II) carbonic anhydrase-sulphonamide complexes. Biochem. J. *143*, 703–715.

28. Bertini, I., Canti, G., Luchinat, C., and Scozzafava, A. (1978). Characterization of

cobalt(II) bovine carbonic anhydrase and of its derivatives. J. Am. Chem. Soc. *100*, 4873–4877.

29. Saliba, D., Ammar, M., Rammal, M., Al-Ghoul, M., and Hmadeh, M. (2018). Crystal Growth of ZIF-8, ZIF-67, and Their Mixed-Metal Derivatives. J. Am. Chem. Soc. *140*, 1812–1823.

30. Yeung, H.H.-M., Sapnik, A.F., Massingberd-Mundy, F., Gaultois, M.W., Wu, Y., Fraser, D.A.X., et al. (2019). Control of Metal-Organic Framework Crystallization by Metastable Intermediate Pre-equilibrium Species. Angew. Chem. Int. Ed. *58*, 566–571.

31. Férey, G., Haouas, M., Loiseau, T., and Taulelle, F. (2014). Nanoporous Solids: How Do They Form? An In Situ Approach. Chem. Mater. *26*, 299–309.

32. Moh, P.Y., Cubillas, P., Anderson, M.W., and Attfield, M.P. (2011). Revelation of the molecular assembly of the nanoporous metal organic framework ZIF-8. J. Am. Chem. Soc. *133*, 13304–13307.

33. Biswal, D., and Kusalik, P.G. (2017). Probing Molecular Mechanisms of Self-Assembly in Metal-Organic Frameworks. ACS Nano *11*, 258–268.

34. O'Brien, M.G., Beale, A.M., and Weckhuysen, B.M. (2010). The role of synchrotron radiation in examining the self-assembly of crystalline nanoporous framework materials: from zeolites and aluminophosphates to metal organic hybrids. Chem. Soc. Rev. *39*, 4767–4782.

35. Aerts, A., Kirschhock, C.E.A., and Martens, J.A. (2010). Methods for in situ spectroscopic probing of the synthesis of a zeolite. Chem. Soc. Rev. *39*, 4626–4642.

36. Lupulescu, A.I., and Rimer, J.D. (2014). In situ imaging of silicalite-1 surface growth reveals the mechanism of crystallization. Science *344*, 729–732.

37. Weckhuysen, B.M., Baetens, D., and Schoonheydt, R.A. (2000). Spectroscopy of the Formation of Microporous Transition Metal Ion Containing Aluminophosphates under Hydrothermal Conditions. Angew. Chem. Int. Ed. Engl. *39*, 3419–3422.

38. De Yoreo, J.J., Gilbert, P.U., Sommerdijk, N.A., Penn, R.L., Whitelam, S., Joester, D., et al. (2015). Crystallization by particle attachment in synthetic, biogenic, and geologic environments. Science *349*, aaa6760.

39. Loh, N.D., Sen, S., Bosman, M., Tan, S.F., Zhong, J., Nijhuis, C.A., Král, P., Matsudaira, P., and Mirsaidov, U. (2017). Multistep nucleation of nanocrystals in aqueous solution. Nat. Chem. *9*, 77–82.

40. Venna, S.R., Jasinski, J.B., and Carreon, M.A. (2010). Structural evolution of zeolitic imidazolate framework-8. J. Am. Chem. Soc. *132*, 18030–18033.

41. Ogata, A.F., Rakowski, A.M., Carpenter, B.P., Fishman, D.A., Merham, J.G., Hurst, P.J., and Patterson, J.P. (2020). Direct Observation of Amorphous Precursor Phases in the Nucleation of Protein-Metal-Organic Frameworks. J. Am. Chem. Soc. *142*, 1433–1442.

42. Xing, J., Schweighauser, L., Okada, S., Harano, K., and Nakamura, E. (2019). Atomistic structures and dynamics of prenucleation clusters in MOF-2 and MOF-5 syntheses. Nat. Commun. *10*, 3608.

43. Surblé, S., Millange, F., Serre, C., Férey, G., and Walton, R.I. (2006). An EXAFS study of the formation of a nanoporous metal-organic framework: evidence for the retention of secondary building units during synthesis. Chem. Commun. (Camb.) (14), 1518–1520.

44. Cantu, D.C., McGrail, B.P., and Glezakou, V.-A. (2014). Formation Mechanism of the Secondary Building Unit in a Chromium Terephthalate Metal–Organic Framework. Chem. Mater. *26*, 6401–6409.

45. Rood, J.A., Boggess, W.C., Noll, B.C., and Henderson, K.W. (2007). Assembly of a homochiral, body-centered cubic network composed of vertex-shared Mg12 cages: use of electrospray ionization mass spectrometry to monitor metal carboxylate nucleation. J. Am. Chem. Soc. *129*, 13675–13682.

46. Avrami, M. (1939). Kinetics of Phase Change. I General Theory. J. Chem. Phys. *7*, 1103–1112.

47. Gualtieri, A.F. (2001). Synthesis of sodium zeolites from a natural halloysite. Phys. Chem. Miner. *28*, 719–728.

48. Schäfer, P., Kapteijn, F., van der Veen, M.A., and Domke, K.F. (2017). Understanding the Inhibiting Effect of BTC on CuBTC Growth through Experiment and Modeling. Cryst. Growth Des. *17*, 5603–5607.

49. Frisch, M.J., Trucks, G.W., Schlegel, H.B., Scuseria, G.E., Robb, M.A., Cheeseman, J.R., Scalmani, G., Barone, V., Mennucci, B., Petersson, G.A., et al. (2016). Gaussian 16 (Gaussian, Inc.).

50. Hutter, J., Iannuzzi, M., Schiffmann, F., and VandeVondele, J. (2014). cp2k: atomistic simulations of condensed matter systems. Wiley Interdiscip. Rev. Comput. Mol. Sci. *4*, 15–25.

51. Tribello, G.A., Bonomi, M., Branduardi, D., Camilloni, C., and Bussi, G. (2014). PLUMED 2: New feathers for an old bird. Comput. Phys. Commun. *185*, 604–613.